Original Article

Machine Learning Approach and Model for Predicting Proton Stopping Power Ratio and Other Parameters Using Computed Tomography Images

Charles Ekene Chika
Department of Mathematics, University of Nigeria, Nsukka, Enugu State, Nigeria

Abstract

Purpose: The purpose of this study was to accurately estimate proton stopping power ratio (SPR), relative electron density ρ_e, effective atomic number (Z_{eff}), and mean excitation energy (I) using one simple robust model and design a machine learning algorithm that will lead to automation. **Methods:** Empirical relationships between computed tomography (CT) number and SPR, ρ_e (Z_{eff}) and I were used to formulate a model that predicts all the four parameters using linear attenuation coefficients which can be converted to CT numbers. The results of these models were compared with the results of other existing models. Thirty-three ICRU human tissues were used as modeling data and 12 Gammex inserts as testing data for the machine learning algorithm designed. More ways of tissue classification were introduced to improve accuracy. In the examples, the dual energy methods were implemented using 80 kVp and 150 kVP/Sn. **Results:** The proposed method gave modeling root mean square error (RMSE) near 1% at maximum for the case of SPR and ρ_e for both single and dual-energy CT approaches considered with modeling RMSE of 0.32% for ρ_e and 0.38% for SPR as modeling RMSE with room for improvement (this can be done by adjusting the model number of terms as well as the parameters). The method was able to achieve modeling RMSE of 1.11% for I and 1.66% for Z_{eff}. The mean error for all the estimated quantities was near 0.00%. In most cases, the proposed method has lower testing RMSE and mean error compare to the other methods presented in the study. **Conclusion:** The proposed method proves to be more flexible and robust among all presented methods since it has lower testing error in most cases and can be improved based on data using the machine learning algorithm. The algorithm can also improve estimation by adjusting the model as well as aid in automation and it's easy to implement.

Keywords: Empirical computation, machine learning, mathematical model, optimization, proton stopping power ratio, radiation therapy

Received on: 16-07-2024 **Review completed on:** 20-10-2024 **Accepted on:** 21-10-2024 **Published on:** 18-12-2024

Introduction

The treatment of tumors using proton therapy is gaining popularity as more treatment centers are being built around the globe. Protons have an advantage over photons as a result of its Bragg peak depth-dose curve; to make good use of this property, there is a need for accurate estimation of proton range which depends on the stopping power ratio (SPR). This leads to the study on how to effectively compute proton SPR and other parameters it depends on directly or indirectly such as the relative electron density ρ_e, effective atomic number (Z_{eff}), and mean excitation energy (I).

The current state-of-the-art method in use is the single energy computed tomography (SECT) stoichiometric calibration method which has been studied by several research groups. A range uncertainty margin of 3%–3.5% is added to the distal boundary of the clinical target volume for the proton range due to SECT uncertainties in computing the proton range.[1-3] Factors like CT number uncertainties which can be caused by beam hardening and CT image noise have a large effect on this method; therefore, studies have investigated dual-energy CT (DECT) approaches to help mitigate these uncertainties.

DECT makes use of CT images acquired at two different energies to estimate SPR in the case of image domain methods,

Address for correspondence: Dr. Charles Ekene Chika,
Department of Mathematics, University of Nigeria, Nsukka,
Enugu State, Nigeria.
E-mail: charles.chika@unn.edu.ng

Access this article online

Quick Response Code:

Website:
www.jmp.org.in

DOI:
10.4103/jmp.jmp_120_24

How to cite this article: Chika CE. Machine learning approach and model for predicting proton stopping power ratio and other parameters using computed tomography images. J Med Phys 2024;49:519-30.

whereas the CT projection data are used to estimate the SPR in the case of projection domain methods. Many models and methods have been developed by different groups like those presented by Hünemohr *et al*.,[4] Bourque *et al*.,[5] Williams *et al*., and other methods.[6-32,33-45,46-50] Empirical approaches have been studied as well like the one presented by Taasti *et al*.[22] Uncertainties of some of these methods have been studied, for example, Yang *et al*..[12] conducted this study and showed that the DECT method was more robust to uncertainties that might be due to change in tissue composition, change in position compared to the SECT method. Furthermore, a good two-energy combination for the DECT method has been studied[47] where they found that spectral separation contributes to the accuracy of the estimation. The projection domain has been studied using different approaches like the one done by Shuangyue *et al*.[2,8] and others. The projection domain shows improved performance but requires high computation skills like the multi-energy approach proposed by Shen *et al*.[9] Some methods aimed at improving projection domain computation are still under development like the one presented by Chika and Hooshyar.[51]

Current studies are looking on how to improve the accuracy of these methods, improve the computation efficiency, and aid in automation which leads to the present study.

This study presents an image domain multienergy model based on empirical relationships which will help improve accuracy and reduce the uncertainties. Developed machine learning algorithm based on the model that will help in the automation of the computation process. We also carried out the comparison of the presented model with some other existing models and methods that follow similar ideas directly or indirectly. Theoretical linear attenuation coefficients of tissues (which can be converted to theoretical CT numbers) were used to estimate proton SPR, relative electron density ρ_e, effective atomic number (Z_{eff}), and mean excitation energy (I).

Materials and Methods

Computed tomography data preparation

The mixture rule was applied to elemental mass attenuation coefficients gotten from the National Institute of Standards and Technology (NIST) XCOM database to compute linear attenuation coefficients.[52] The CT number of each pixel in CT images for unknown tissue was represented by:

$$\frac{<\mu>_{S_i}}{<\mu_w>_{S_i}} \approx \frac{HU_{S_i}}{1000}+1, \tag{1}$$

where μ_w, μ are the linear attenuation coefficients of water and unknown tissue, respectively. $S_i = 1, 2$ represents low- and high-energy spectra, respectively. Eq (1) is by convention. We assume that a phantom consisting of unknown compounds or mixtures was scanned with a commercial CT scanner at low- ($S_i = 1$) and high-energy ($S_i = 2$) spectra, characterized by normalized X-ray energy fluence spectra ϕ_{Si} (E) where $\int_E \phi_{S_i}(E)dE = 1$.

$$\frac{<\mu>_{S_i}}{<\mu_w>_{S_i}} = \frac{\int_E \phi_{S_i}(E)\mu(xE)dE}{\int_E \phi_{S_i}(E)\mu_w(xE)dE}, \tag{2}$$

For simplicity, we adopt the following notation

$$\frac{<\mu>_{S_i}}{<\mu_w>_{S_i}} = <\frac{\mu}{\mu_w}>_{S_i} = \mu_{S_i}.$$

This is the theoretical linear attenuation used for this study which can be applied to Eq (1) to get the CT number.

The energy spectra are computed using SpekCalc[53,54] and its normalized form is presented in Figure 1.

Tissue classification

33 ICRU human tissues are used for this study[55-58,59,60-62] Appendix]. The tissues are classified into three groups which are lung, soft, and bone tissues; this is the popularly used classification. We also considered the case of splitting the soft tissue into two, making it four groups [Figure 2]. This grouping is done here using the $f_L = \mu_1$ and $f_r(\mu) = \frac{\mu_1}{\mu_2}$, respectively. The boundaries that separate each group are shown in Figure 3 (lung if $f_L \leq 0.3$, soft if $f_L \leq 1.4$, and bone if $f_L \leq 1.4$) and Figure 2, respectively.

These human tissues were used as training data and the 12 Gammex insert tissues were used as testing data.

Proposed method

Given a radiological parameter p related to the attenuation coefficient μ, there exist transformations/maps $T(p)$ and $f(\mu)$ such that:

$$T(p) = \sum_{i=-j}^{n} (a_i\, f(\mu))^{(i)} + err \tag{3}$$

$n \geq 0, j \geq 0$ and $p = T^{-1}(T(p))$

$a_i \in \Re$, where, $\mu = (\mu_1, \mu_2, \mu_{3,...,} \mu_m)$ for n-energies ($n \geq 1$) with at least one low energy (that is $\leq 90kVp$) and err is an acceptable error.

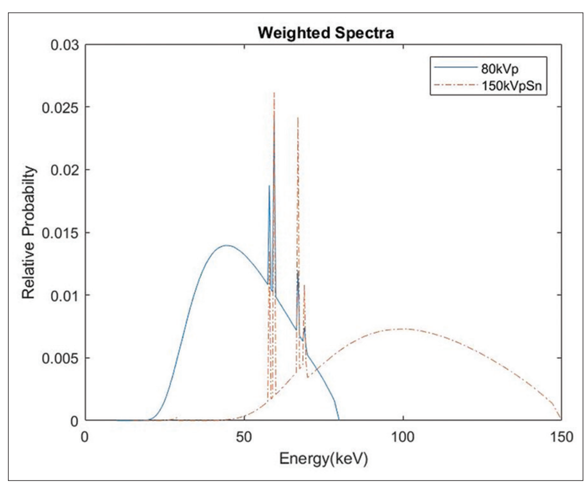

Figure 1: Specra used

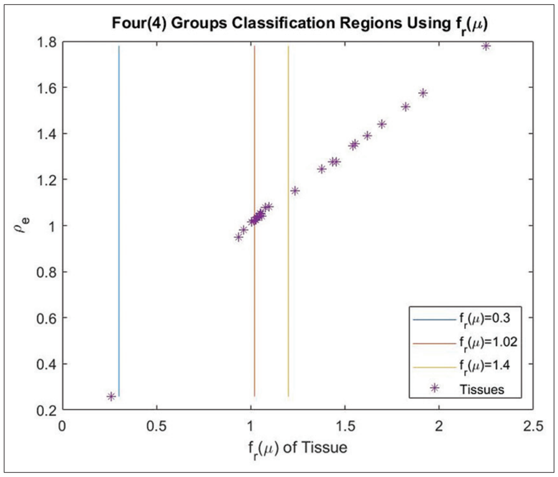

Figure 2: 4 Regions of classification (lung tissues if $f_L \leq 0.3$, soft tissue 1 if $0.3 < fr \leq 1.02$, soft tissue 2 if $1.02 < fr \leq 1.4$, and bone tisue if $f_L > 1.4$)

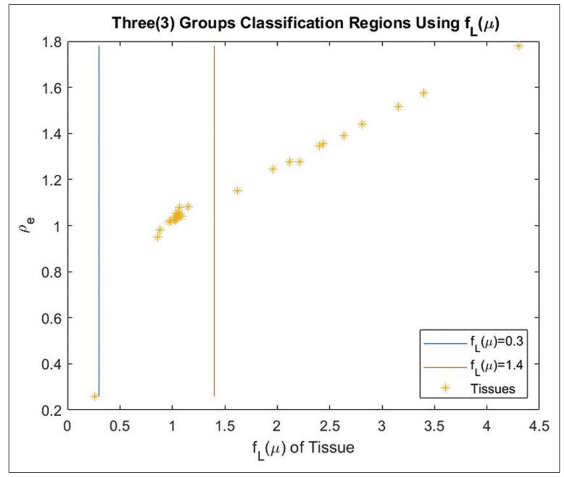

Figure 3: 3 Regions of classification (lung tissues if $f_L \leq 0.3$, soft tissue if $0.3 < f_L \leq 1.4$, and bone tisue if $f_L > 1.4$

The low energy requirement is based on the observation made during the study.

The relationship is found using data observation approach like plotting to see how the data are related, after which reasonable $f(\mu)$ is constructed and a good approach of estimating the constants is employed.

$$T(p) \approx \sum_{i=-j}^{n} (a_i(f(\mu))^i = a_{-j}(f(\mu))^{-j} + \ldots + a_{-1}(f(\mu))^{-1} + a_0(f(\mu))^0 + a_1(f(\mu))^1 + \ldots + a_n(f(\mu))^n.$$

where, $a_{-j}(f(\mu))^{-j} = \dfrac{a_{-j}}{(f(\mu))^j}$

We used two energies for this study commonly known as dual energy. Three $f(\mu)$ were used which are: $f_L(\mu) = \mu_1$, $f_r(\mu) = \dfrac{\mu_1}{\mu_2}$, $f_m(\mu) = \mu_1 \times \mu_2$.

T $(p) = p$ for ρ_e and SPR, T $(p) = \ln(p)$ for I and Z_{eff}. We implemented the simple form of the model,

$$T(p) = \sum_{i=-1}^{n} a_i f^i(\mu) \tag{4}$$

$n = 0$ for (I) and Z_{eff}. On ρ_e and SPR, $n = 0$ for soft tissues and $n = 2$ for bone tissues.

Symbol Definition: $T_{p,j,n}$ here means T for parameter p, low index $-j$, and top index n. Example:

$$T_{p,1,2} = \sum_{i=-1}^{2} (a_i f(\mu))^i$$

Stopping power ratio

For the range of energy mostly used in proton therapy, the proton SPR can be approximated by the Bethe–Bloch equation

$$SPR = \rho_e \frac{ln\dfrac{2m_e c^2 \beta^2}{1-\beta^2} - \beta^2 - lnI}{ln\dfrac{2m_e c^2 \beta^2}{1-\beta^2} - \beta^2 - lnI_w} \tag{5}$$

where m_e is the rest mass of an electron, c is the speed of light, β is the velocity of the proton in vacuum relative to the speed of light, and I_w (approximately 75.3) is the mean excitation energy of water.

We compute our reference SPR using the Eq (5) at 175 MeV proton energy. Some of the considered examples from our method are as below and the model parameters, a_i, are given in the Supplementary Tables 1-3.

$$T_{SPR,1,1} = \begin{cases} a_0, & Lung \\ \dfrac{a_{-1}}{f(\mu)} + a_0, & Soft \\ \dfrac{a_{-1}}{f(\mu)} + a_0, & Bone \end{cases}$$

$$T_{SPR,1,2} = \begin{cases} a_0, & Lung \\ \dfrac{a_{-1}}{f(\mu)} + a_0, & Soft \\ \dfrac{a_{-1}}{f(\mu)} + a_0 + a_1 f(\mu) + a_2 f(\mu), & Bone \end{cases}$$

We considered the following methods and compared them with our proposed method for the case of SPR.

Stochiometric method

Here, we are referring to single-energy CT which is currently in use for planning. The single energy calibration method[13] uses single energy CT attenuation to estimate SPR through linear piece-wise function, i.e.

$$SPR = \begin{cases} a_l, & lung \\ a_s \mu + b_s, & soft \\ a_b \mu + b_b, & bone \end{cases} \quad (6)$$

where $\alpha_l = 0.2579$, $\alpha_s = 0.3343$, $b_s = 0.6939$, $a_b = 0.9283$ and $b_b = 0.0780$ with the data described in section 2.1.

This is the same as what we will denote as $T_{SPR,0,1}$ in our method, so stochiometric calibration is just a subset of our proposed method. We implemented this model using low energy μ i.e., μ_l.

Hünemohr–Saito method

Hünemohr *et al*.[4] developed the model below and Saito has previously developed a similar formula for ρ_e. This model is what we refer to as Hünemohr–Saito (H-S) method.

$$\frac{\rho_e}{\rho_{e,w}} = a_H \mu_1 + (1 - a_H)\mu_2 \quad (7)$$

$$Z_{eff} = \left(\left(\frac{\rho_e}{\rho_{e,w}}\right)^{-1} (b_H \mu_1 + (Z_{e,w}^n - b_H)\mu_2)\right)^{\frac{1}{n}} \quad (8)$$

The two model parameters, α_H and b_H, depend on specific dual-energy scanning protocols. Here, it is computed theoretically with the data described in section 2.1; for soft tissues $\alpha_H = 0.594$, $b_H = 3.6348$ and $n = 0.6379$, whereas for bone tissues $\alpha_H = -0.1457$, $b_H = 1.2493$, and $n = 0.6807$. To estimate SPR from the values of ρ_e and Z_{eff} images, Hünemohr used the empirical relationship between I-value and Z_{eff} which was first introduced by Yang *et al*.[12] We used this with classification based on the attenuation as stated below to fit into the classification of our study.

$$\ln(I) = \begin{cases} a_l, & \mu_L \le 0.3 \\ a_s Z_{eff} + b_s, & \mu_L \le 1.4 \\ a_b Z_{eff} + b_b, & \mu_L > 1.4 \end{cases} \quad (9)$$

where $\alpha_l = 4.3197$, $a_s = 0.0865$, $b_s = 3.6374$, $a_b = 0.0495$ and $b_b = 3.8345$.

Taasti method

The empirical parametrization model presented by Taasti *et al*.. using dual-energy is stated below.

$$SPR_{soft}^{est} = \left[(1 + a_1^t)\mu_2 - a_1^t \mu_1\right] + a_2^t \mu_1^2 + a_3^t \mu_2^2 + a_4^t (\mu_1^3 + \mu_2^3) \quad (10)$$

$$SPR_{bone}^{est} = \left[(1 + a_1^t)\mu_2 - a_1^t \mu_1\right] + a_2^t \frac{\mu_1}{\mu_2} + a_3^t (\mu_1^2 - \mu_2^2) + a_4^t (\mu_1^3 + \mu_2^3) \quad (11)$$

We used our classification to implement this. For soft tissue, $a_1^t = 2.3826$, $a_2^t = 2.8450$ $a_3^t = -1.3042$ and $a_4^t = -0.7695$, whereas for bone tissues $a_1^t = 0.9517$, $a_2^t = 0.0388$, $a_3^t = 0.2829$ and $a_4^t = -0.0258$.

Relative electron density (ρ_e)

We computed reference relative electron density using the following formula:

$$\rho_e = \frac{\rho_{e,x}}{\rho_{e,w}} = \frac{\rho_x \sum_{m=1}^{M} \frac{\omega_m Z_m}{A_m}}{\rho_{e,w}} \quad (12)$$

where ρ_x denotes the mass density. ω_m, Z_m, and A_m are the mass fraction, atomic number, and atomic mass of the *m-th* element in the tissue, respectively. The proposed methods are compared with the H-S method stated in the previous section. The model examples are as below and the model parameters, a_i, are in Supplementary Tables 4-6.

$$T_{\rho_e,1,1} = \begin{cases} a_0, & Lung \\ \frac{a_{-1}}{f(\mu)} + a_0, & Soft \\ \frac{a_{-1}}{f(\mu)} + a_0, & Bone \end{cases}$$

$$T_{\rho_e,1,2} = \begin{cases} a_0, & Lung \\ \frac{a_{-1}}{f(\mu)} + a_0, & Soft \\ \frac{a_{-1}}{f(\mu)} + a_0 + a_1 f(\mu) + a_2 f(\mu), & Bone \end{cases}$$

Effective atomic number Z_{eff}

Effective atomic number was computed with the Mayneord's equation as stated below.

$$Z^l = \frac{\sum_m^M \frac{\omega_m Z_m}{A_m} Z_m^l}{\sum_m^M \frac{\omega_m Z_m}{A_m} Z_m} \quad (13)$$

where Z_m is the atomic number of the *m-th* element and $l = 3.3$. This was used as the reference Z_{eff}.

We used $T_{\mu L}$ and $T_{\mu r}$ for $ln\ (Z_{eff})$, whereas $T_{\mu m}$ was used for Z_{eff}

The implemented example is:

$$T_{Z,1,1} = \begin{cases} a_0, & Lung \\ \frac{a_{-1}}{f(\mu)} + a_0, & Soft \\ \frac{a_{-1}}{f(\mu)} + a_0, & Bone \end{cases}$$

The model parameters, a_i, are presented in Supplementary Tables 7 and 8.

Bourque's model

In Bourque's model, spectrally averaged elemental electronic cross sections are fit to polynomial function, $<\sigma_e>(Z) = \sum_k^K a_k Z^{k-1}$, of their atomic number, Z, The spectrally-dependent effective atomic number for an arbitrary mixture is then defined as:

$Z_{eff} = <\sigma_e>^{-1}\left(\sigma_{e,mixture}\right)$. The parametric $\rho_e - Z_{eff}$ model is given by:

$$Z_{eff} = \sum_{k=1}^{K} (a_k \frac{\mu_1 - \mu_2}{\mu_1 + \mu_2})^{(k-1)} \tag{14}$$

$$\frac{\rho_e}{\rho_{e,w}} = \frac{\mu_{\frac{L}{H}}}{\sum_{m=1}^{M} d_{m,\frac{L}{H}} Z^{m-1}} \tag{15}$$

where a_k and $d_{m,L/H}$ are scanner-specific model parameters. The scanner-specific parameters are determined theoretically from a calibration phantom. The original study used $K = M = 6$ which is also used here.

We couldn't implement Bourque's model because we didn't have cross-section data handy. Hence, we just implemented the Z_{eff} as in our model and that's what we represented as $T_{B,0,1}$.

$$T_{B,0,1} = \sum_{k=1}^{K} (a_k f(\mu))^{(k-1)} \tag{16}$$

where, $f(\mu) = \frac{\mu_1 - \mu_2}{\mu_1 + \mu_2}$; for soft tissues $a_1 = 7.1$, $a_2 = 24.2$, $a_3 = -47.9$, $a_4 = -1108.3$, $a_5 = -10.9$ and 68.1, whereas for bone tissues $a_1 = 15$, $a_2 = 142$, $a_3 = 1523$, $a_4 = -6921$, $a_5 = 14817$ and $a_6 = -12140$.

Mean excitation energy *I* (ev)

The Bragg additivity rule was used to compute the mean excitation energy for each tissue:

$$\ln(I) = \frac{\sum_m (\omega_m \frac{Z}{A})_m \ln(I_m))}{\sum_m (\omega_m \frac{Z}{A})_m} \tag{17}$$

I_m is the mean excitation energy of the *m-th* element in the tissue.

We used the presented classification and the Yang's empirical relationship between Z_{eff} and I on H-S method for the purpose of comparison since we can't find any model that predicts mean excitation energy directly from the attenuation coefficients.

We used $T_{\mu L}$ and $T_{\mu r}$ for ln(I), whereas Tμm was used for I.

The implemented example is:

$$T_{I,1,1} = \begin{cases} a_0, & Lung \\ \frac{a_{-1}}{f(\mu)} + a_0, & Soft \\ \frac{a_{-1}}{f(\mu)} + a_0, & Bone \end{cases}$$

The model parameters, a_i, are presented in Supplementary Tables 9 and 10.

Accuracy analysis

$$ME = \frac{1}{N}\sum_{i=1}^{N} err_i \tag{18}$$

$$RMSE = \sqrt{\frac{\sum_{i=1}^{N} err_i^2}{N}} \tag{19}$$

$$err = \frac{p_{Ref} - p_{est}}{p_{Ref}} \tag{20}$$

The mean error measures the overall bias of the values estimates, whereas the RMSE error measures the systematic estimation error for different tissues.

Results

Stopping power ratio

Table 1 shows that the proposed method $T_{SPR,1,2}$;*fL*(μ) defined using *fr*(μ) gives the overall least modeling RMSE when the tissues are grouped into three categories while that defined using *fm*(μ) gave the least testing RMSE for DECT. The implemented model from the proposed single energy CT method ($T_{SPR,1,2}$;*fL*(μ)) performed slightly better than the existing stoichiometric method both in testing and modeling error, it also gave the least testing error for the presented methods. The H-S method gave the largest modeling error, whereas the Taasti method gave the largest testing error. Further classification into four groups gave a better modeling error since it reduced the error of $T_{SPR,1,2}$ defined using *fr*(μ) from 0.49 to 0.38 but not necessarily a better testing error.

We see from Table 2 that all the methods except H-S, $T_{SPR,1,2}$;*fr*(μ) and $T_{SPR,1,2}$;*fr*(μ) have very little bias in modeling but a slightly higher bias in testing. From Figures 4 and 5, we observe that $T_{SPR,1,2}$ performed relatively better than other methods in modeling bone tissues and has overall least mean error.

Relative electron density

Just as in the case of SPR, Table 3 shows that the proposed method, $T_{\rho e,1,2}$;*fr*(μ), defined using *fr*(μ) gives the overall least modeling RMSE when the tissues are grouped into three categories while that defined using *fm*(μ) gives the least testing RMSE for DECT. The proposed single energy CT model ($T_{SPR,1,2}$;*fL*(μ)) gave overall least testing error. The H-S method gave the largest modeling error. Further classification into four groups gives a better modeling error since it reduced the error of $T_{\rho e,1,2}$ defined using *fr*(μ) from 0.37 to 0.32 but not necessarily a better testing error.

We see from Table 4 that all the proposed methods have very little bias compared to the H-S method in modeling but bias increased in testing data. From Figure 6, we observe that $T_{\rho e,1,2}$ performed relatively better than other methods in modeling soft and bone tissues.

Table 1: Stopping power ratio modeling and testing root mean square (%)

SPR modelling RMSE	Total	Lung	Soft	Bone	Testing RMSE	Total	Soft	Bone
$T_{SPR,1,1}$; $f_r(\mu)$	1.78	0.04	0.58	2.98		4.72	4.80	4.61
$T_{SPR,1,2}$; $f_r(\mu)$	0.49	0.04	0.58	0.26		5.87	4.82	7.08
$T_{SPR,1,2}$; $f_m(\mu)$	1.04	0.03	1.14	0.87		3.89	3.07	4.80
$T_{SPR,1,2}$; $f_L(\mu)$	0.85	0.00	1.00	0.53		3.14	3.28	3.27
Stochiometric	0.86	0.01	1.00	0.56		3.39	3.35	3.44
Taasti	0.60	0.01	0.22	1.00		6.77	7.19	6.14
H−S	5.10	0.45	3.42	7.46		4.51	4.47	4.57
$T_{SPR,1,2}$; $f_r(\mu)$ 4 g	0.38	0.04	0.44	0.26		5.87	4.82	7.08

SPR: Stopping power ratio, RMSE: Root mean square

Table 2: Stopping power ratio modeling and testing mean error (%)

SPR modelling ME	Total	Lung	Soft	Bone	Testing ME	Total	Soft	Bone
$T_{SPR,1,1}$; $f_r(\mu)$	0.28	0.04	0.01	0.84		0.63	1.02	0.09
$T_{SPR,1,2}$; $f_r(\mu)$	0.00	0.04	0.00	0.00		−0.05	1.06	−1.62
$T_{SPR,1,2}$; $f_m(\mu)$	−0.09	−0.03	−0.02	−0.24		−2.08	−1.48	−2.92
$T_{SPR,1,2}$; $f_L(\mu)$	0.00	0.00	−0.01	0.02		−1.04	−0.85	−1.30
Stochiometric	−0.01	−0.01	−0.01	−0.01		−1.15	−0.93	−1.46
Taasti	−0.02	−0.01	−0.01	−0.03		2.19	2.95	1.14
H−S	0.17	0.45	2.25	−3.84		−0.23	2.66	−4.28
$T_{SPR,1,2}$; $f_r(\mu)$ 4 g	0.00	0.04	0.00	0.00		−0.31	0.62	−1.62

SPR: Stopping power ratio, ME: Mean error

Table 3: ρ_e modeling and testing root mean square (%)

ρ_e modelling RMSE	Total	Lung	Soft	Bone	Testing RMSE	Total	Soft	Bone
$T_{\rho e,1,1}$; $f_r(\mu)$	1.03	0.2	0.45	1.67		4.60	4.69	4.46
$T_{\rho e,1,2}$; $f_r(\mu)$	0.37	0.2	0.41	0.29		6.04	4.94	7.32
$T_{\rho e,1,2}$; $f_m(\mu)$	1.08	−0.05	1.14	1.03		4.06	3.05	5.15
$T_{\rho e,1,2}$; $f_L(\mu)$	0.81	−0.2	0.92	0.59		3.04	3.00	3.10
H−S	5.14	0.01	3.16	7.76		5.00	4.34	5.79
$T_{\rho e,1,2}$; $f_r(\mu)$ 4 g	0.32	0.02	0.35	0.29		6.00	4.85	7.32

RMSE: Root mean square

Table 4: ρ_e modeling and testing mean error (%)

ρ_e modeling ME	Total	Lung	Soft	Bone	Testing ME	Total	Soft	Bone
$T_{\rho e,1,1}$; $f_r(\mu)$	0.02	0.02	0.02	0.02		0.54	0.94	−0.01
$T_{\rho e,1,2}$; $f_r(\mu)$	0.00	0.2	0.01	−0.01		−0.05	1.32	−1.97
$T_{\rho e,1,2}$; $f_m(\mu)$	−0.12	−0.05	−0.03	−0.30		−2.63	−2.03	−3.46
$T_{\rho e,1,2}$; $f_L(\mu)$	−0.01	−0.2	−0.01	−0.01		−1.23	−0.99	−1.56
H−S	−0.28	0.01	1.81	−4.30		−1.00	1.98	−5.18
$T_{\rho e,1,2}$; $f_r(\mu)$ 4 g	0.00	0.02	0.00	−0.01		−0.19	1.08	−1.97

ME: Mean error

Table 5: Z_{eff} modeling and testing root mean square (%)

Z_{eff} modelling RMSE	Total	Lung	Soft	Bone	Testing RMSE	Total	Soft	Bone
$T_{Z,1,1}$; $f_r(\mu)$	2.47	0.00	3.03	0.88		4.69	5.08	4.07
$T_{Z,1,1}$; $f_m(\mu)$	2.06	0.00	2.48	0.95		6.51	8.02	3.42
$T_{Z,1,1}$; $f_L(\mu)$	1.66	0.00	2.06	0.46		4.29	5.26	2.34
$T_{B,0,1}$	2.87	0.00	3.00	2.77		4.86	4.78	4.99
H−S	10.61	0.00	2.87	17.95		14.63	2.77	22.43
$T_{Z,1,1}$; $f_r(\mu)$ 4 g	2.24	0.00	2.73	0.88		5.69	6.61	4.07

RMSE: Root mean square

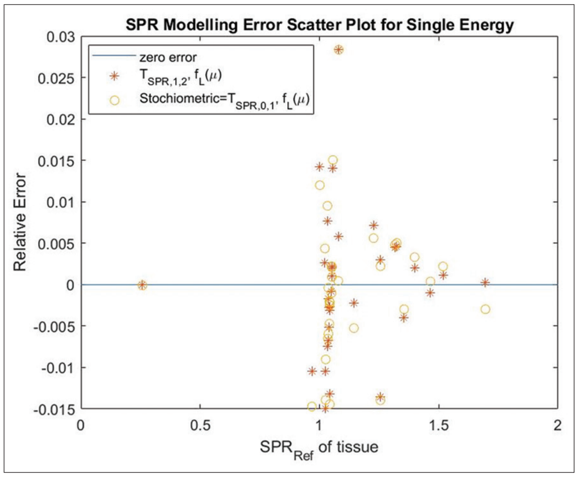

Figure 4: Individual tissues stopping power ratio relative error for the presented single energy methods

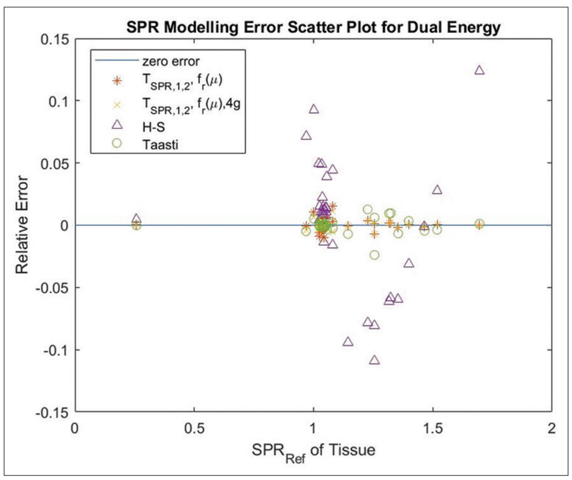

Figure 5: Individual tissues stopping power ratio relative error for the presented dual energy methods

Effective atomic number

Table 5 shows that the proposed single low-energy model outperforms all other ones in both modeling and testing data. $T_{Z,1,1}$ defined using $fm(\mu)$ gave the least modeling RMSE when the tissues were grouped into three categories, whereas the one defined on $fr(\mu)$ gave the least testing RMSE among dual energy methods. The proposed single energy model gave overall least testing error. The H-S method gave the largest modeling error and testing error. Further classification into four groups only shows slight improvement in modeling error.

We see from Table 6 that all the proposed methods have very little bias compared to the H-S method in modeling and some of the proposed models still maintained relatively low bias in testing data. From Figure 7, we observed that $T_{Z,1,1}$, $f_L(\mu)$ performed relatively better than other methods in modeling soft and bone tissues.

Mean excitation energy

Table 7 shows that although H-S has slightly lower modeling RMSE, $T_{Z,1,1}$ defined using $fr(\mu)$ gave the least modeling RMSE when the tissues were grouped into three categories. Further classification into four groups shows improvement in modeling error since it reduces the error from 1.64 to 1.11 but don't show improvement in testing error.

Table 8 indicates that all the methods have very little bias in modeling and relatively increased bias in testing data. From Figure 8, we observed that some of the proposed methods achieved similar results in modeling soft and bone tissues.

Discussion

The model that can be used to estimate some of the important treatment parameters in radiotherapy is presented. Unlike most models including some of the ones presented here that are restricted to single or dual energy the one proposed can be applied to any number (n) of energies; we just need to construct suitable T_μ for the energies. The method is based on empirical knowledge and it's validated using a theoretical poly-energy attenuation coefficient. This implies that it takes the energy spectrum into account as well as other properties of the phantom or machine. This is not saying that it takes care of the uncertainties associated with those situations in practice as different detailed studies are needed to ascertain that. We can make the model more general by including the case where the parameter we are interested in depends on other known parameters and not just the attenuation coefficient from the given CT image data. The model will be as stated below.

A generalized version of the proposed method: given a radiological parameter p related to the attenuation coefficient μ and some other parameters p', there exist transformations/maps $T(p)$ and $f(\mu,p')$ such that

$$T(p) = \sum_{i=-j}^{n} (a_i f(\mu, p'))^{(i)} + err \tag{21}$$

$n \geq 0, j \geq 0$ and $p = T^{-1}\left(T\left(p\right)\right)$

$a_i \in \Re$, where, $\mu = \left(\mu_1, \mu_2, \mu_3, \ldots, \mu_n\right)$ for n-energies with at least one low energy, $p' = \left(p'_1, p'_2, p'_3, \ldots, p'_K\right)$ for K-known parameters and *err* is an acceptable error.

A similar idea of this model has been applied in estimating SPR and I using electron density[13] but what we presented here estimates the parameters directly from the CT image.

We talk about classification because it contributes a lot to accuracy. For example, one of the T_μ we tried that's not presented here and gave reasonable RMSE but gives a high error for spongiosa and sacrum which were more than 6% and 3%, respectively. When these two tissues were classified as soft tissues instead of bone tissues, their error reduced

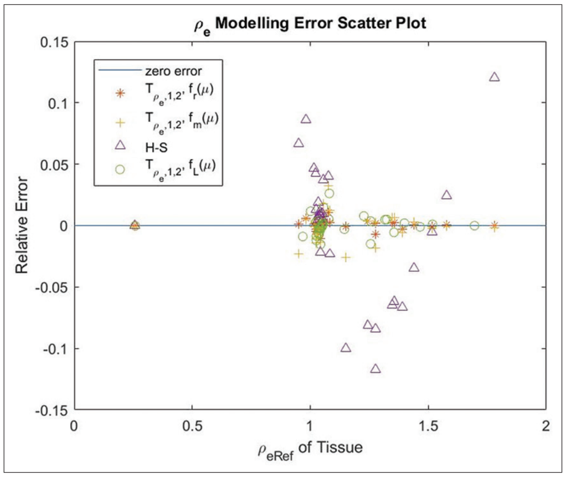

Figure 6: Individual tissues ρ_e relative error for the presented methods on computing relative electron density

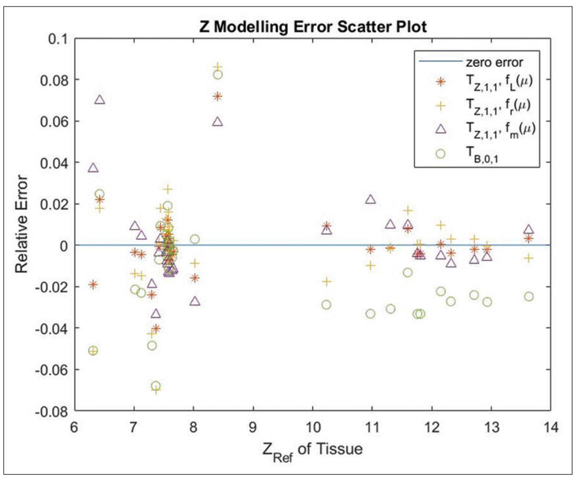

Figure 7: Individual tissues Z_{eff} relative error for the presented methods on computing the effective atomic number

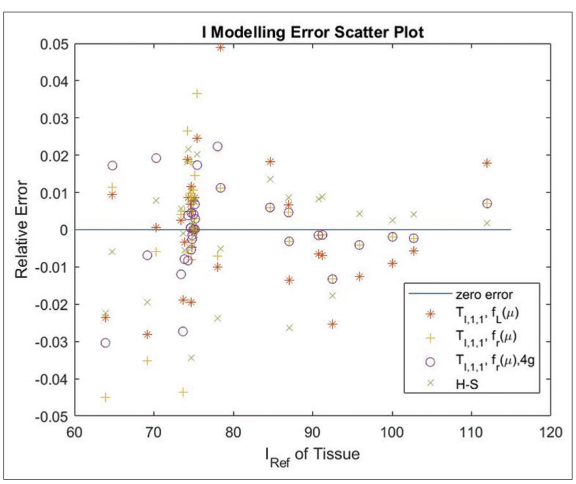

Figure 8: Individual tissues *I* relative error for the presented methods on computing mean excitation energy

tremendously with that of sacrum reducing to near 1% and spongiosa reducing to −0.04%. Grouping the tissues into more classes instead of two classes also improves the results as shown in tables and figures by splitting soft tissues further into two making it four groups at least improves the modeling error. Further careful classification can be done using any preferred $f(\mu)$, it has to be carefully done because of our next discussion.

In general, the model proposed here works well and has a lot of opportunities for improvement especially based on the classification, function construction, and degree of fitting. Caution needs to be taken in other to avoid overfitting and over smoothing. For example, looking at Figure 4 and Table 1 for SPR, $T_{SPR,1,1}$;$fr(\mu)$ has total modeling RMSE of 1.78% (soft 0.58%, bone 2.98%) which are reduced to total modeling error of 0.49% (bone 0.26%) for $T_{SPR,1,2}$;$fr(\mu)$ with increasing *n* degree fitting from 1 to 2. Observe what is happening in the testing error, it moved from a total testing error of 4.72% (bone 4.61% to total testing error of 5.87% (bone 7.08%). This actually gets worse testing error indicating overfitting of the data or over smoothing of the function. Similarly, $T_{SPR,1,2}$;$fr(\mu)$ 4*g* which is grouping the tissues into four categories instead of three categories with the same increased fitting degree improved the modeling error but not the testing. Similar results hold for ρ_e.

The method beats many of the existing methods, especially on estimating *Z* and *I* with the theoretical attenuation coefficient. Although we couldn't access a method that estimates mean excitation energy directly from the attenuation coefficient of the CT image, we compared it with the H-S method combined with the empirical relationship presented by Yang *et al*.[12] Yang *et al*. empirical approach is just referred to for comparison purposes since the presented method estimates mean excitation energy directly from the given CT image data unlike theirs that has to estimate effective atomic number first.

The limitation of this study is the limited data since the machine learning approach needs a lot of data to improve accuracy but we were able to make the optimal use of the data we have. The study can be considered a little bit ambitious compared to the idea that has been in existence, which is modifying tissue composition a little and checking for uncertainty. We used Gammex tissues as our testing tissues so the difference in error is expected.

The machine learning algorithm for the proposed method can be written as follows:

Determine the needed parameter $p = SPR, \rho e, I, Zeff, ...$
(i) Given CT image data
(ii) Compute μ
(iii) Check the empirical relationship between p and μ
(iv) If an empirical relationship exists, construct T_μ
(v) Formulate T_p
(vi) Classify the tissues
(vii) Estimate the model parameters a_i
(viii) Check the modeling and testing error
(ix) Repeat iv-viii until optimal acceptable error is reached given more priority to testing error.

Table 6: Z_{eff} modeling and testing mean error (%)

Z modeling ME	Total	Lung	Soft	Bone	Testing ME	Total	Soft	Bone
$T_{Z,1,1}; f_r(\mu)$	−0.04	0.00	−0.04	−0.02		2.39	4.81	−1.00
$T_{Z,1,1}; f_m(\mu)$	0.10	0.00	0.07	0.16		1.33	0.73	2.17
$T_{Z,1,1}; f_L(\mu)$	0.00	0.00	−0.01	0.02		1.21	1.10	1.36
$T_{B,0,1}$	−1.21	0.00	−0.49	−2.71		1.59	4.69	−3.39
H−S	−6.74	0.00	−1.92	−16.56		−5.95	−0.24	−13.95
$T_{Z,1,1}; f_r(\mu)$ 4 g	−0.03	0.00	−0.04	−0.02		3.16	6.13	−1.00

ME: Mean error

Table 7: *I* modeling and testing root mean square (%)

I modeling RMSE	Total	Lung	Soft	Bone	Testing RMSE	Total	Soft	Bone
$T_{I,1,1}; f_r(\mu)$	1.64	0.01	2.00	0.64		4.06	4.36	3.60
$T_{I,1,1}; f_m(\mu)$	2.90	0.00	3.27	2.17		5.93	6.73	4.56
$T_{I,1,1}; f_L(\mu)$	1.55	0.01	1.32	1.97		5.86	5.65	6.13
H−S	1.33	0.00	1.44	1.16		6.75	5.03	8.60
$T_{I,1,2}; f_r(\mu)$ 4 g	1.11	0.01	1.31	0.64		4.31	4.76	3.60

RMSE: Root mean square

Table 8: *I* modeling and testing mean error (%)

I modeling ME	Total	Lung	Soft	Bone	Testing ME	Total	Soft	Bone
$T_{I,1,1}; f_r(\mu)$	−0.01	0.01	−0.02	0.01		0.01	1.91	−2.66
$T_{I,1,1}; f_m(\mu)$	−0.17	0.00	−0.19	−0.15		−3.88	−4.88	−2.48
$T_{I,1,1}; f_L(\mu)$	0.03	0.01	−0.02	0.11		−0.65	−1.39	0.38
H−S	0.00	0.00	−0.01	0.03		−2.64	−2.11	−3.39
$T_{I,1,2}; f_r(\mu)$ 4 g	0.00	0.01	−0.01	0.01		0.98	3.59	−2.66

ME: Mean error

Conclusion

The proposed method achieved modeling RMSE as low as 0.85% on single energy and 0.38% on dual energy for SPR and all RMSE are near 1% at maximum. Similarly, modeling RMSE as low as 0.81% on single energy and 0.32% on dual energy were achieved for ρ_e and all RMSE are near 1% at maximum. In the same vein, the model achieved good accuracy for Z_{eff} and *I*. The mean errors are all close to 0.00%. This method is more robust compared to other methods considered in this study since it mostly has lower errors on testing data using theoretical CT numbers. It also provides the flexibility to improve accuracy using any number of energy spectrum (n-energy).

The machine learning algorithm provides opportunity for automation and improvement. The algorithm provided will help improve the accuracy of predicting SPR, $\rho_{e,}$ *I* and Z_{eff} by considering models with different degrees, different tissue classifications, and different CT data. Both the model and the algorithm are easy and flexible to implement as they can be used to estimate different parameters with same set of data.

Data availability statements

The mass attenuation coefficients used for this study were gotten from NIST XCOM database which can be found with this link https://www.nist.gov/pml/xcom-photon-cross-sections-database. The tissue linear attenuation is gotten using the tissue composition, summing over weighted spectrum and multiplying the mass attenuation with its linear density.

Elemental composition for different tissues can be found in,[55-58] ICRU database, or any other trusted source.

We use the formulas in materials and methods section and the tissues elemental composition to compute the relative electron density, mean excitation energy, effective atomic number and SPR for each tissue.

The spectra used are computed using SpekCalc.[54]

Some of these, data can be provided under reasonable request.

Financial support and sponsorship

Nil.

Conflicts of interest

There are no conflicts of interest.

References

1. Taasti VT, Bäumer C, Dahlgren CV, Deisher AJ, Ellerbrock M, Free J, *et al.* Inter-centre variability of CT-based stopping-power prediction in particle therapy: Survey-based evaluation. Phys Imaging Radiat Oncol 2018;6:25-30.
2. Zhang S, Han D, Politte DG, Williamson JF, O'Sullivan JA. Impact of joint statistical dual-energy CT reconstruction of proton stopping

power images: Comparison to image- and sinogram-domain material decomposition approaches. Med Phys 2018;45:2129-42.
3. Park PC, Zhu XR, Lee AK, Sahoo N, Melancon AD, Zhang L, *et al*. A beam-specific planning target volume (PTV) design for proton therapy to account for setup and range uncertainties. Int J Radiat Oncol Biol Phys 2012;82:e329-36.
4. Hünemohr N, Krauss B, Tremmel C, Ackermann B, Jäkel O, Greilich S. Experimental verification of ion stopping power prediction from dual energy CT data in tissue surrogates. Phys Med Biol 2014;59:83-96.
5. Bourque AE, Carrier JF, Bouchard H. A stoichiometric calibration method for dual energy computed tomography. Phys Med Biol 2014;59:2059-88.
6. Lee HH, Park YK, Duan X, Jia X, Jiang S, Yang M. Convolutional neural network based proton stopping-power-ratio estimation with dual-energy CT: A feasibility study. Phys Med Biol 2020;65:215016.
7. Lee HH, Li B, Duan X, Zhou L, Jia X, Yang M. Systematic analysis of the impact of imaging noise on dual-energy CT-based proton stopping power ratio estimation. Med Phys 2019;46:2251-63.
8. Zhang S, Han D, Williamson JF, Zhao T, Politte DG, Whiting BR, *et al.* Experimental implementation of a joint statistical image reconstruction method for proton stopping power mapping from dual-energy CT data. Med Phys 2019;46:273-85.
9. Shen C, Li B, Lou Y, Yang M, Zhou L, Jia X. Multienergy element-resolved cone beam CT (MEER-CBCT) realized on a conventional CBCT platform. Med Phys 2018;45:4461-70.
10. Paganetti H. Range uncertainties in proton therapy and the role of Monte Carlo simulations. Phys Med Biol 2012;57:R99-117.
11. Yang M, Virshup G, Clayton J, Zhu XR, Mohan R, Dong L. Theoretical variance analysis of single- and dual-energy computed tomography methods for calculating proton stopping power ratios of biological tissues. Phys Med Biol 2010;55:1343-62.
12. Yang M, Zhu XR, Park PC, Titt U, Mohan R, Virshup G, *et al.* Comprehensive analysis of proton range uncertainties related to patient stopping-power-ratio estimation using the stoichiometric calibration. Phys Med Biol 2012;57:4095-115.
13. Schneider U, Pedroni E, Lomax A. The calibration of CT Hounsfield units for radiotherapy treatment planning. Phys Med Biol 1996;41:111-24.
14. Bär E, Lalonde A, Royle G, Lu HM, Bouchard H. The potential of dual-energy CT to reduce proton beam range uncertainties. Med Phys 2017;44:2332-44.
15. Bazalova M, Carrier JF, Beaulieu L, Verhaegen F. Dual-energy CT-based material extraction for tissue segmentation in Monte Carlo dose calculations. Phys Med Biol 2008;53:2439-56.
16. Saito M. Potential of dual-energy subtraction for converting CT numbers to electron density based on a single linear relationship. Med Phys 2012;39:2021-30.
17. Landry G, Seco J, Gaudreault M, Verhaegen F. Deriving effective atomic numbers from DECT based on a parameterization of the ratio of high and low linear attenuation coefficients. Phys Med Biol 2013;58:6851-66.
18. Hünemohr N, Paganetti H, Greilich S, Jäkel O, Seco J. Tissue decomposition from dual energy CT data for MC based dose calculation in particle therapy. Med Phys 2014;41:061714.
19. Garcia LI, Azorin JF, Almansa JF. A new method to measure electron density and effective atomic number using dual-energy CT images. Phys Med Biol 2016;61:265-79.
20. Lalonde A, Bouchard H. A general method to derive tissue parameters for Monte Carlo dose calculation with multi-energy CT. Phys Med Biol 2016;61:8044-69.
21. Farace P. Experimental verification of ion stopping power prediction from dual energy CT data in tissue surrogates. Phys Med Biol 2014;59:7081-4.
22. Taasti VT, Petersen JB, Muren LP, Thygesen J, Hansen DC. A robust empirical parametrization of proton stopping power using dual energy CT. Med Phys 2016;43:5547.
23. Saito M, Sagara S. Simplified derivation of stopping power ratio in the human body from dual-energy CT data. Med Phys 2017;44:4179-87.
24. Kanematsu N, Inaniwa T, Koba Y. Relationship between electron density and effective densities of body tissues for stopping, scattering, and nuclear interactions of proton and ion beams. Med Phys 2012;39:1016-20.
25. Li B, Lee HC, Duan X, Shen C, Zhou L, Jia X, *et al.* Comprehensive analysis of proton range uncertainties related to stopping-power-ratio estimation using dual-energy CT imaging. Phys Med Biol 2017;62:7056-74.
26. Saito M, Tsukihara M. Technical note: Exploring the limit for the conversion of energy subtracted CT number to electron density for high atomic number materials. Med Phys 2014;41:071701.
27. Alvarez RE, Macovski A. Energy-selective reconstructions in X-ray computerized tomography. Phys Med Biol 1976;21:733-44.
28. Lehmann LA, Alvarez RE, Macovski A, Brody WR, Pelc NJ, Riederer SJ, *et al.* Generalized image combinations in dual KVP digital radiography. Med Phys 1981;8:659-67.
29. Chuang K-S, Huang H. Comparison of four dual energy image decom- position methods. Phys Med Biol 1988;33:455-66.
30. Schlomka JP, Roessl E, Dorscheid R, Dill S, Martens G, Istel T, *et al.* Experimental feasibility of multi-energy photon-counting K-edge imaging in pre-clinical computed tomography. Phys Med Biol 2008;53:4031-47.
31. Han D, Siebers JV, Williamson JF. A linear, separable two-parameter model for dual energy CT imaging of proton stopping power computation. Med Phys 2016;43:600.
32. Han D, Porras-Chaverri MA, O'Sullivan JA, Politte DG, Williamson JF. Technical note: On the accuracy of parametric two-parameter photon cross-section models in dual-energy CT applications. Med Phys 2017;44:2438-46.
33. Zhang S, Han D, Politte D, Porras-Chaverri M, Whiting B, Williamson J, *et al*. Basis vector model based method for proton stopping power estimation from experimental dual energy CT data. Med Phys 2016;43:3756.
34. Zhang S, Han D, Politte DG, Williamson JF, O'Sullivan JA. Compar- ison of integrated and post-reconstruction dual-energy ct proton stop- ping power ratio estimation approaches. Med Phys 2017;44:3004.
35. Bethe H. Zur theorie des durchgangs schneller korpuskularstrahlen durch materie. Ann Phys 1930;397:325-400.
36. Williamson JF, Li S, Devic S, Whiting BR, Lerma FA. On two-parameter models of photon cross sections: Application to dual-energy CT imaging. Med Phys 2006;33:4115-29.
37. Herman GT, Trivedi SS. A comparative study of two postreconstruction beam hardening correction methods. IEEE Trans Med Imaging 1983;2:128-35.
38. Herman GT. Correction for beam hardening in computed tomography. Phys Med Biol 1979;24:81-106.
39. Evans JD, Whiting BR, Politte DG, O'Sullivan JA, Klahr PF, Williamson JF. Experimental implementation of a polyenergetic statistical reconstruction algorithm for a commercial fan-beam CT scanner. Phys Med 2013;29:500-12.
40. Whiting BR. Signal statistics in X-ray computed tomography. Proc. SPIE 4682. Med Imag 2002;4682:53-60.
41. Lasio GM, Whiting BR, Williamson JF. Statistical reconstruction for x-ray computed tomography using energy-integrating detectors. Phys Med Biol 2007;52:2247-66.
42. Csisaar I. Why least squares and maximum entropy? an axiomatic approach to inference for linear inverse problems. Ann Stat 1991;19:2032-66.
43. Williamson JF, Whiting BR, Benac J, Murphy RJ, Blaine GJ, O'Sullivan JA, *et al.* Prospects for quantitative computed tomography imaging in the presence of foreign metal bodies using statistical image reconstruction. Med Phys 2002;29:2404-18.
44. Stevenson R, Delp E. Fitting Curves with Discontinuities. In: Proc. The First International Workshop on Robust Computer Vision; 1990. p. 127-36.
45. Degirmenci S, Politte DG, Bosch C, Tricha N, O'Sullivan JA. Acceleration of iterative image reconstruction for X ray imaging for security applications. In: Proc. SPIE 9401. Comput Imag XIII, 2015. 94010C.
46. Evans JD, Politte DG, Whiting BR, O'Sullivan JA, Williamson JF. Noise-resolution tradeoffs in x-ray CT imaging: A comparison of penalized alternating minimization and filtered backprojection algorithms. Med Phys 2011;38:1444-58.
47. Yang M, Virshup G, Clayton J, Zhu XR, Mohan R, Dong L. Does

kV-MV dual-energy computed tomography have an advantage in determining proton stopping power ratios in patients? Phys Med Biol 2011;56:4499-515.
48. Berger MJ, Hubbell JH, Seltzer SM, Chang J, Coursey JS, Sukumar R, *et al*. XCOM: Photon Cross Section Database. Ver.1.3. 2005.
49. Yang M, Virshup G, Mohan R, Shaw CC, Zhu XR, Dong L. Improving accuracy of electron density measurement in the presence of metallic implants using orthovoltage computed tomography. Med Phys 2008;35:1932-41.
50. Flohr TG, McCollough CH, Bruder H, Petersilka M, Gruber K, Süss C, *et al.* First performance evaluation of a dual-source CT (DSCT) system. Eur Radiol 2006;16:256-68.
51. Chika CE, Hooshyar MA. An electromagnetic inverse scattering problem for dielectrics that depend on two spatial variables via eikonal approximation. Microw Opt Technol Lett 2019;61:1517-23. [doi: 10.1002/ mop.31752].
52. Berger MJ, Hubbell JH, Seltzer SM, Chang J, Coursey JS, Sukumar R, *et al*. XCOM: Photon Cross Section Data-Base. Ver. 1.5. Gaithersburg, MD: National Institute of Standards and Technology; 2010.
53. Birch R, Marshall M. Computation of bremsstrahlung X-ray spectra and comparison with spectra measured with a Ge(Li) detector. Phys Med Biol 1979;24:505-17.
54. Poludniowski G, Landry G, DeBlois F, Evans PM, Verhaegen F. SpekCalc: A program to calculate photon spectra from tungsten anode x-ray tubes. Phys Med Biol 2009;54:N433-8.
55. White DR, Woodard HQ, Hammond SM. Average soft-tissue and bone models for use in radiation dosimetry. Br J Radiol 1987;60:907-13.
56. White DR, Widdowson EM, Woodard HQ, Dickerson JW. The composition of body tissues (II). Fetus to young adult. Br J Radiol 1991;64:149-59.
57. Woodard HQ. The composition of human cortical bone: Effect of age and of some abnormalities. Clin Orthop Relat Res 1964;37:187-93.
58. Woodard HQ, White DR. The composition of body tissues. Br J Radiol 1986;59:1209-18.
59. Chika CE. Estimation of proton stopping power ratio and mean excitation energy using electron density and its applications via machine learning approach. J Med Phys 2024;49:155-66.
60. ICRU. Tissue Substitutes in Radiation Dosimetry and Measurement. Report No. 44. ICRU, Bethesda, MD; 1989.
61. ICRU. Stopping Powers for Electrons and Positrons. Report No. 37 ICRU, Bethesda, MD; 1984.
62. ICRU. Stopping Power and Ranges for Protons and Alpha Particles ICRU Report No 49 (Bethesda, MD: ICRU); 1993.

Appendix

33 ICRU tissues used:

Lung (Inflated), Yellow marrow, Adipose, Breast, Red marrow, Eye lens, Skin, Pancreas, GI tract, Testis, Lymph, Kidney, Ovary, Muscles, Brain, Liver, Spleen, Lung (Deflated), Heart (blood filled), Blood, Cartilage, Thyroid, Spongiosa, Sacrum, Vertebral (D6, L3), Femur, Ribs (2nd, 6th), Vertebral C4, Humerus, Ribs (10th), Cranium, Mandible, Cortical bone.

Gammex inserts used:

Adipose (Gammex), Breast (Gammex), True water (Gammex), Solid water (Gammex), Muscle (Gammex), Brain (Gammex), Liver (Gammex), Inner bone (Gammex), B200 (Gammex), CB30 (Gammex), CB50 (Gammex), Cortical bone (Gammex).

Supplementary Table 1: Stopping power ratio a_i's value for f_r (μ)

$T_{SPR,1,1}$; f_r (μ)	a_{-1}	a_0	a_1	a_2	$T_{SPR,1,2}$	a_{-1}	a_0	a_1	a_2
Lung ≤0.3	0	0.2578	0	0		0	0.2578	0	0
Soft ≤1.2	−0.6689	1.6858	0			−0.6689	1.6858	0	0
Bone	−1.707	2.4267	0	0		0.0533	0.3327	0.654	−0.026

SPR: Stopping power ratio

Supplementary Table 2: Stopping power ratio a_i's value for f_m (μ) and f_L (μ)

$T_{SPR,1,2}$; f_L (μ)	a_{-1}	a_0	a_1	a_2	$T_{SPR,1,2}$; f_m (μ)	a_{-1}	a_0	a_1	a_2
Lung ≤0.3	0	0.2579	0	0	≤0.3	0	0.2580	0	0
Soft ≤1.4	−0.325	1.356	0	0	≤1.5	−0.2068	1.2416	0	0
Bone	0.0531	0.7277	0.2485	−0.062		0.2186	0.7936	0.1353	−0.0035

Supplementary Table 3: 4 groups stopping power ratio a_i's value for f_r (μ)

$T_{SPR,1,2}$; f_r (μ)	a_{-1}	a_0	a_1	a_2
Lung ≤0.3	0	0.2578	0	0
Soft 1 ≤1.02	−0.7028	1.7247	0	0
Soft 2 ≤1.2	−0.913	1.9178	0	0
Bone	0.0533	0.3327	0.654	−0.026

Supplementary Table 4: ρ_e a_i's value for f_r (μ)

$T_{\rho e,1,1}$; f_r (μ)	a_{-1}	a_0	a_1	a_2	$T_{\rho e,1,2}$	a_{-1}	a_0	a_1	a_2
Lung ≤0.3	0	0.2578	0	0		0	0.2578	0	0
Soft ≤1.2	−0.7619	1.7723	0	0		−0.8275	1.835	0	0
Bone	−1.9515	2.615	0	0		0.042	0.2633	0.7193	−0.0235

Supplementary Table 5: ρ_e a_i's value for f_m (μ) and T_L (μ)

$T_{\rho e,1,2}$; $T_{\mu L}$	a_{-1}	a_0	a_1	a_2	$T_{\rho e,1,2}$; $T\mu m$	a_{-1}	a_0	a_1	a_2
Lung ≤0.3	0	0.2579	0	0	≤0.3	0	0.2580	0	0
Soft ≤1.4	−0.4098	1.4344	0	0	≤1.5	−0.2289	1.26	0	0
Bone	0.0559	0.6820	0.2801	−0.0065		0.2745	0.7357	0.1568	−0.0041

Supplementary Table 6: 4 groups ρ_e a_i's for f_r (μ)

$T_{\rho e,1,2}$; f_r (μ)	a_{-1}	a_0	a_1	a_2
Lung ≤0.3	0	0.2578	0	0
Soft 1 ≤1.02	−0.8155	1.826	0	0
Soft 2 ≤1.2	−0.9732	1.9744	0	0
Bone	0.042	0.2633	0.7193	−0.0235

Supplementary Table 7: Z_{eff} a_i's value for f_L (μ), f_r (μ) and f_m (μ)

$T_{Z,1,1}$; f_L (μ)	a_{-1}	a_0	$T_{Z,1,1}$; f_r (μ)	a_{-1}	a_0	$T_{Z,1,1}$; f_m (μ)	a_{-1}	a_0
Lung ≤0.3	0	2.0278	≤0.3	0	2.0278	≤0.3	0	7.5975
Soft ≤1.4	−0.9039	2.8844	≤1.2	−1.5785	3.5317	≤2.5	−5.3520	12.682
Bone	−0.7612	2.7856		−0.7585	3.5317		−11.817	14.967

Supplementary Table 8: 4 groups Z_{eff} a_i's value for f_r (μ)

$T_{Z,1,1}$; $T_{\mu r}$	a_{-1}	a_0
Lung ≤0.3	0	2.0278
Soft 1 ≤1.02	−1.401	3.3352
Soft 2 ≤1.2	−0.8698	2.8591
Bone	−0.7585	2.956

Supplementary Table 9: *I* a_i's value for f_L (μ), f_r (μ) and f_m (μ)

$T_{I,1,1}$; f_L (μ)	a_{-1}	a_0	$T_{I,1,1}$; f_r (μ)	a_{-1}	a_0	$T_{I,1,1}$; f_m (μ)	a_{-1}	a_0
Lung ≤0.3	0	4.3196	≤0.3	0	4.3196	≤0.3	0	75.1668
Soft ≤1.4	−0.7124	4.9869	≤1.2	−1.2954	5.5466	≤3	−12.804	85.899
Bone	−1.0087	4.9344		−0.9906	5.1517		−131.45	125.95

Supplementary Table 10: 4 groups *I* a_i's Value for f_r (μ)

$T_{I,1,1}$; f_r (μ)	a_{-1}	a_0
Lung ≤0.3	0	4.3196
Soft 1 ≤1.02	−1.0436	5.271
Soft 2 ≤1.2	−0.4726	4.7658
Bone	−0.9906	5.1517